Post-starburst Galaxies in the Centers of Intermediate-redshift Clusters

Ariel Werle, Bianca Poggianti, Alessia Moretti, Callum Bellhouse, Benedetta Vulcani, Marco Gullieuszik, Mario Radovich, Jacopo Fritz, Alessandro Ignesti, Johan Richard, et al.

The Astrophysical Journal, 930:43 (15pp), 2022 May 1 https://doi.org/10.3847/1538-4357/ac5f06

Post-starburst Galaxies in the Centers of Intermediate-redshift Clusters

Ariel Werle[1], Bianca Poggianti[1], Alessia Moretti[1], Callum Bellhouse[1], Benedetta Vulcani[1], Marco Gullieuszik[1], Mario Radovich[1], Jacopo Fritz[2], Alessandro Ignesti[1], Johan Richard[3], Geneviève Soucail[4], Gustavo Bruzual[2], Stephane Charlot[5], Matilde Mingozzi[6], Cecilia Bacchini[1], Neven Tomicic[1], Rory Smith[7], Andrea Kulier[1], Giorgia Peluso[1,8], and Andrea Franchetto[1,8]

[1] INAF-Osservatorio Astronomico di Padova, Vicolo Osservatorio 5, I-35122 Padova, Italy; ariel.werle@inaf.it
[2] Instituto de Radioastronomía y Astrofísica, Universidad Nacional Autónoma de México, Morelia, Michoacán, 58089 México
[3] Univ Lyon, ENS de Lyon, CNRS, Centre de Recherche Astrophysique de Lyon UMR5574, F-69230 Saint-Genis-Laval, France
[4] Institut de Recherche en Astrophysique et Planétologie (IRAP), Université de Toulouse, CNRS, UPS, CNES,14 Av. Edouard Belin, F-31400 Toulouse, France
[5] Sorbonne Universités, UPMC-CNRS, UMR7095, Institut d'Astrophysique de Paris, F-75014, Paris, France
[6] Space Telescope Science Institute, 3700 San Martin Drive, Baltimore, MD 21218, USA
[7] Departamento de Física, Universidad Técnica Federico Santa María, Avenica Vicuña Mackenna 3939, San Joaquín, Santiago, Chile
[8] Dipartimento di Fisica e Astronomia "G. Galilei", Universit`a di Padova, Vicolo dell'Osservatorio 3, I-35122 Padova, Italy
Received 2021 December 9; revised 2022 March 16; accepted 2022 March 16; published 2022 May 3

Abstract

We present results from MUSE spatially resolved spectroscopy of 21 post-starburst galaxies in the centers of eight clusters from $z \sim 0.3$ to $z \sim 0.4$. We measure spatially resolved star formation histories (SFHs), the time since quenching (t_Q), and the fraction of stellar mass assembled in the past 1.5 Gyr ($\mu_{1.5}$). The SFHs display a clear enhancement of star formation prior to quenching for 16 out of 21 objects, with at least 10% (and up to >50%) of the stellar mass being assembled in the past 1.5 Gyr and t_Q ranging from less than 100 to ∼800 Myr. By mapping t_Q and $\mu_{1.5}$, we analyze the quenching patterns of the galaxies. Most galaxies in our sample have quenched their star formation from the outside in or show a side-to-side/irregular pattern, both consistent with quenching by ram pressure stripping. Only three objects show an inside-out quenching pattern, all of which are at the high-mass end of our sample. At least two of them currently host an active galactic nucleus. In two post-starbursts, we identify tails of ionized gas indicating that these objects had their gas stripped by ram pressure very recently. Post-starburst features are also found in the stripped regions of galaxies undergoing ram pressure stripping in the same clusters, confirming the link between these classes of objects. Our results point to ram pressure stripping as the main driver of fast quenching in these environments, with active galactic nuclei playing a role at high stellar masses.

Unified Astronomy Thesaurus concepts: Galaxy environments (2029); Galaxy evolution (594); Galaxy clusters (584); Post-starburst galaxies (2176); E+A galaxies (424)

1. Introduction

Post-starburst (also known as k+a or E+A) galaxies are a population of galaxies undergoing a rapid transition from star-forming to quiescent. These objects were first identified as a distinct population in clusters at intermediate redshift (Dressler & Gunn 1983; Couch & Sharples 1987) but have since been recognized in a variety of environments and redshifts (e.g., Poggianti et al. 2004). Post-starbursts are usually identified by their strong Balmer absorption lines and lack of emission lines associated with star formation (e.g., Dressler et al. 1999; Poggianti et al. 1999; Goto 2007), although recently other selection methods have been developed (e.g., Wild et al. 2007, 2014; Belli et al. 2019; see French 2021 for a description of various selection criteria). These characteristic spectral features indicate significant levels of star formation in the recent past (∼1–1.5 Gyr) but no ongoing star formation, indicating fast quenching sometime in the recent past.

There is strong evidence that post-starbursts were more common at higher redshifts in all environments. In fact, D'Eugenio et al. (2020) have recently shown that the stacked spectrum of nine massive quiescent field galaxies at $z \sim 3$ has clear post-starburst features. Wild et al. (2009) find that the number density of post-starbursts decreases by a factor of 200 from $z \sim 0.7$ to $z \sim 0.07$ and that they account for 38^{+4}_{-11}% of the growth of the red sequence at $0.5 < z < 1.0$. Post-starbursts represent less than 1% of the field galaxy population at $z \sim 0.5$ and more than 5% at $z \sim 2$ (Wild et al. 2016). Using a different approach, Belli et al. (2019) found that 34% of quiescent galaxies are post-starbursts at $z \sim 2.5$, while at $z \sim 1$ they are only 4%. Fritz et al. (2014) found that the fraction of bright post-starbursts in clusters decreases from 18% at redshifts $0.37 < z < 0.56$ to 4.6% at $0.04 < z < 0.07$. The mass function of post-starburst galaxies also evolves with redshift in all environments, shifting toward lower masses at lower redshift according to a downsizing trend (Poggianti et al. 2004; Wild et al. 2016).

Post-starburst galaxies are also known to favor denser environments, being more common in clusters (Poggianti et al. 2009; Dressler et al. 2013; Paccagnella et al. 2017, 2019; Wilkinson et al. 2021). The main process responsible for fast quenching in these environments seems to be ram pressure stripping. For example, Poggianti et al. (2009) find a correlation between the fraction of post-starbursts and the cluster velocity dispersion. This correlation establishes a link between the rapid quenching of star formation and the properties of the intracluster medium (ICM) as ram pressure stripping becomes more efficient in more massive clusters. A perhaps more direct evidence of this connection is found by Poggianti et al. (2004), who identify a spatial correlation between post-starbursts and substructures of the hot ICM detected using X-ray data from XMM-Newton. When studying cluster galaxies in the GAs Stripping Phenomena in

galaxies (GASP; Poggianti et al. 2017) survey, Vulcani et al. (2020) found that the star formation histories (SFHs) and location within the cluster of rapidly quenched galaxies are consistent with quenching by ram pressure stripping. Furthermore, Gullieuszik et al. (2017) and Poggianti et al. (2019) showed that regions of jellyfish galaxies (i.e., galaxies with long tails of gas stripped by ram pressure) that were already stripped of gas have spectral features typical of post-starburst galaxies, further suggesting that galaxies undergoing ram pressure stripping could be the progenitors of post-starbursts.

In the field and group environments, post-starbursts are usually associated with other processes, most commonly galaxy interactions and mergers. Simulations show that gas-rich major mergers can lead to centrally concentrated starbursts, followed by a post-starburst phase and significant morphological transformation (Bekki et al. 2005; Wild et al. 2009; Snyder et al. 2011; Pawlik et al. 2019; Zheng et al. 2020). These features are consistent with several observational studies of field/group post-starbursts (Blake et al. 2004; Pawlik et al. 2018; Chen et al. 2019; D'Eugenio et al. 2020). Using spatially resolved spectroscopy from the Mapping Nearby Galaxies at Apache Point Observatory (MaNGA; Bundy et al. 2015) survey, Rowlands et al. (2018) found that more asymmetric galaxies have a larger fraction of post-starburst spaxels, which also favors the merger hypothesis. Most post-starbursts in the field have a spheroidal morphology expected of merger remnants (Blake et al. 2004; Pawlik et al. 2018), while cluster post-starbursts have more prominent disks that indicate quenching through a process that does not significantly disturb the structure of the stellar disk, such as ram pressure stripping (Dressler et al. 1999; Tran et al. 2003).

Post-starbursts are also known to be connected with feedback from active galactic nuclei (AGNs; Yan et al. 2006; Sanmartim et al. 2013; Pawlik et al. 2018). However, it is unclear if AGNs are efficient enough to be the main driver of quenching (e.g., Kaviraj et al. 2007; Baron et al. 2018) or only prevent any residual star formation from taking place after a main quenching event is triggered by a different process (e.g., Yesuf et al. 2014).

In the local universe, "rejuvenation events" in early-type galaxies (Werle et al. 2020; de Sá-Freitas et al. 2022) triggered by minor mergers can also lead to a post-starburst phase (Dressler et al. 2013; Pawlik et al. 2018). In particular, Pawlik et al. (2018) find that this process is the origin of ∼40% of massive post-starbursts at $z < 0.05$. However, Chauke et al. (2019) find rejuvenated galaxies at $z \sim 0.8$ to have weaker Balmer lines than typical post-starbursts.

Other processes can also lead to the quenching of star formation but act on longer timescales that are inconsistent with the spectral features of post-starbursts. The heating or removal of gas in the circumgalactic medium (CGM; see Tumlinson et al. 2017) via ram pressure or tidal interactions can prevent the accretion of new gas onto galaxy disks, a process referred to as "starvation" (Larson et al. 1980). This leads to the cessation of star formation once the remaining gas in the disk is consumed. Because the gas-depletion times in normal star-forming galaxies are longer than 1 Gyr (Saintonge et al. 2011; de los Reyes & Kennicutt 2019), this effect would lead to a very slow quenching process that cannot produce post-starburst spectra. We note, however, that the gas-depletion times for starburst galaxies are shorter than 1 Gyr (see Kennicutt & De Los Reyes 2021), indicating that the starvation of a starburst galaxy could in principle lead to a post-starburst.

Table 1
Basic Information about the Clusters Studied in This Work

Cluster	Redshift	R.A.	Decl.	σ (km/s)
A2744	0.308	00:14:20.702	−30:24:00.63	1357
A370	0.375	02:39:53.122	−01:34:56.14	1789
MACS J1206.2–0847	0.438	12:06:12.149	−08:48:03.37	1842
MACS J0257.6–2209	0.322	02:57:41.070	−22:09:17.70	1633
RX J1347.5–1145	0.451	13:47:30.617	−11:45:09.51	1097
SMACS J2031.8–4036	0.331	20:31:53.256	−40:37:30.79	1531
SMACS J2131.1–4019	0.442	21:31:04.831	−40:19:20.92	1378
AS1063	0.3458	22:48:43.99	−44:31:50.98	1660

The cumulative effect of weak tidal interactions ("harassment"; Moore et al. 1996) also acts on long timescales and cannot lead to a post-starburst phase.

The extent to which each of these processes contributes to the quenching of star formation in galaxies residing in different environments remains an open topic. In this work, we take advantage of Multi Unit Spectroscopic Explorer (MUSE) data collected by the GTO program to study a sample of post-starburst galaxies using rest-frame optical spatially resolved spectroscopy of the central regions of intermediate-redshift clusters ($0.308 < z < 0.451$). This allows us to study how fast quenching happens in different regions of galaxies in dense environments, as has been previously done for field and group galaxies (e.g., Rowlands et al. 2018; Chen et al. 2019; D'Eugenio et al. 2020).

The paper is organized as follows. Section 2 describes the data set and the sample selection. Our spectral synthesis method is described in Section 3 and results from the synthesis are presented in 4. In Section 5 we present some special cases of post-starbursts with distinct features in their emission-line maps. Further clues on ram pressure stripping are presented in Section 6 and conclusions are laid out in Section 7.

We assume a standard ΛCDM cosmology with $\Omega_M = 0.3$, $\Omega_\Lambda = 0.7$, and $h = 0.7$. We adopt the solar metallicity value of $Z_\odot = 0.017$ and a Chabrier (2003) initial mass function. The chosen epoch for R.A. and decl. is J2000.

2. Data and Sample

2.1. The Data Set

This work is based on MUSE datacubes from the MUSE Lensing Cluster GTO program, which provides deep observations of the central regions of clusters. These fields were originally targeted due to the abundance of gravitationally lensed background sources. The pixel size in the redshift range of our work is ∼1 kpc, while the seeing is 1″ (∼4–5 kpc). The cluster sample is extracted from a multitude of surveys, including the MAssive Clusters Survey (MACS; Ebeling et al. 2001), the Frontier Fields program (FFs; Lotz et al. 2017), the Grism Lens-Amplified Survey from Space (GLASS; Treu et al. 2015), and the Cluster Lensing And Supernova survey with Hubble (CLASH; Postman et al. 2012). The complete data set is extensively described by Richard et al. (2021).

Here we use data from the clusters A2744, A370, MACS J1206.2–0847, MACS J0257.6–2209, RX J1347.5–1145, SMACS J2031.8–4036, SMACS J2131.1–4019, and Abell S1063. Basic information about these clusters is given in

Table 2
Basic Information about Our Sample of Post-starburst Galaxies

ID	Cluster	Redshift	R.A.	Decl.	$H\delta_A$ (Å)	$H\beta_A$ (Å)	$\log M_\star/M_\odot$
A2744-01	A2744	0.291	00:14:19.754	−30:23:57.83	6.8	8.9	8.9
A2744-02	A2744	0.320	00:14:20.175	−30:23:56.77	4.0	8.5	9.9
A2744-05	A2744	0.307	00:14:18.806	−30:23:13.48	6.2	9.7	9.5
A2744-07	A2744	0.299	00:14:20.474	−30:23:15.10	4.2	8.5	10.2
A2744-08	A2744	0.305	00:14:18.975	−30:24:00.287	4.8	8.0	9.3
A370-04	A370	0.361	02:39:51.370	−1.33.59.091	7.5*	10.4	9.5
A370-05	A370	0.390	02:39:53.544	−01:34:31:751	5.3	10.1	10.0
MACS 1206–06	MACS J1206.2–0847	0.422	12:06:13.17	−08:47:45.05	5.6	9.5	10.7
MACS 1206–09	MACS J1206.2–0847	0.427	12:06:11.36	−08:48:22.0	4.9	11.1	10.4
MACS 1206–11	MACS J1206.2–0847	0.427	12:06:14.856	−08:48:15.6	5.2	9.2	10.5
MACS 0257–01	MACS J0257.6–2209	0.335	02:57:42.581	−22:09:20.61	6.6	10.4	9.2
MACS 0257–03	MACS J0257.6–2209	0.325	02:57:40.15	−22:08:54.4	6.3	8.7	9.5
MACS 0257–04	MACS J0257.6–2209	0.323	02:57:40.7	−22:09:21.6	5.4	7.3	9.6
MACS 0257–05	MACS J0257.6–2209	0.332	02:57:39.9	−22:09:14.2	4.2*	7.8	9.9
RX J1347–02	RX J1347.5–1145	0.431	13:47:31.36	−11:45:50.7	8.5*	11.1	9.9
SMACS 2031–02	SMACS J2031.8–4036	0.329	20:31:51.1	−40:37:21.6	5.0	8.5	10.1
SMACS 2131–05	SMACS J2131.1–4019	0.459	21:31:03.0	−40:19:06.2	4.9*	8.0	9.9
SMACS 2131–06	SMACS J2131.1–4019	0.445	21:31:03.0	−40:19:00.8	4.7*	8.5	9.5
AS1063NE-01	AS1063	0.332	22:48:44.22	−44:31:41.0	5.1	7.6	10.7
AS1063NE-02	AS1063	0.339	22:48:43.11	−44:31:22.98	7.4	10.3	9.8
AS1063SW-01	AS1063	0.326	22:48:40.11	−44:32:04.6	7.4	10.9	9.6

Note. Equivalent widths marked with * were obtained from synthetic spectra

Table 1, where we include the central redshift, position, and velocity dispersion of galaxies in the cluster (σ). Redshifts, positions, and σ were extracted from Richard et al. (2021), except for AS1063, for which these data come from Sartoris et al. (2020) (position and redshift) and Gómez et al. (2012) (σ). The cluster sample is quite massive as it was selected to study gravitational lensing. This characteristic also makes the sample ideal for finding post-starburst galaxies, as the frequency of post-starburst galaxies is known to increase with cluster mass (Poggianti et al. 2009; Dressler et al. 2013; Paccagnella et al. 2019).

For the clusters MACS J0257.6–2209, RX J1347.5–1145, and SMACS J2131.1–4019, observations were carried out using the MUSE adaptive optics system. In these cases the region around ∼5900 Å in the observed frame cannot be used for science due to the NaD notch filter (Stuik et al. 2006).

In addition to the MUSE cubes, we also use images from the Hubble Space Telescope (HST) in the F814W filter, but these are shown only for illustrative purposes in Sections 2.2 and 5.1. These data are taken from the HST archive; for MACS fields, the images are rereduced as presented in Richard et al. (2021).

2.2. Post-starburst Galaxy Sample

As described by Moretti et al. (2022), each datacube was visually inspected to find post-starbursts, as well as the stripped galaxies presented in that paper. Post-starburst galaxies are identified as those generally lacking emission lines but still presenting strong Balmer absorption features anywhere in the stellar disk. After visual inspection, the rest-frame $H\delta$ and $H\beta$ equivalent widths ($H\delta_A$ and $H\beta_A$, respectively) were quantified to confirm the galaxies as post-starburst. We calculate $H\delta_A$ and $H\beta_A$ using the rest-frame spectral regions of 4076–4088 Å and 4806–4826 Å for the blue continuum, 4091–4112 Å and 4826–4896 Å for the lines, and 4117–4136 Å and 4896–4918 Å for the red continuum.

In Table 2 we list some basic information about the 21 post-starbursts in our sample, namely the IDs, cluster names, redshifts, coordinates, $H\delta_A$ and $H\beta_A$ of the integrated spectra, and stellar masses determined using our spectral synthesis procedure (see Section 3). The IDs represent an abbreviation of the cluster name followed by an integer; for AS1063 we also include the acronyms NE (northeast) and SW (southwest) to indicate two different MUSE pointings.

All visually inspected galaxies were confirmed as post-starbursts by comparison with typical criteria from the literature. For most of our sample (14 galaxies), the integrated spectra are above the threshold of $H\delta_A = 5$Å, which is commonly used to select post-starbursts (e.g., Goto 2007; Alatalo et al. 2016); others have slightly lower $H\delta_A$, but are also post-starbursts (k+a) according to the criterion of Poggianti et al. (1999) ($3 < H\delta_A < 5$ Å). Note that for MACS 0257–05, RX J1347–02, and SMACS 2131–06, part of the spectral window required for calculating $H\delta_A$ is unavailable as it is affected by the NaD notch filter. In the case of A370-04, the 5577 Å sky line overlaps with the $H\delta$ region, which brings down the $H\delta_A$ value and makes it unreliable. Nevertheless, for these objects, we report in the table the $H\delta_A$ values measured from the integrated model spectra obtained by SINOPSIS (see Section 3); these are marked with an * on the table. Although $H\delta_A$ is the most commonly used index to select post-starbursts, other Balmer lines can also be used. In cases where $H\delta$ is missing, we confirm the post-starburst nature of the objects by their $H\beta_A$ index ($H\beta_A > 2.5$Å), as done by Vulcani et al. (2020) for Local Cluster galaxies.

The galaxies are distributed in eight clusters and span a redshift range from 0.291 for A2744-01 to 0.459 for SMACS 2131–05. The ages of the universe in these limiting redshifts are 10.1 Gyr and 8.8 Gyr, respectively. Our sample spans a wide range of stellar masses, from $10^{8.9} M_\odot$ for A2744-01 to $10^{10.7} M_\odot$ for MACS 1206–06. We note that our sample typically includes galaxies of low mass, mostly less massive than, e.g., the Milky Way. The low mass indicates that these galaxies could be very quickly stripped by ram pressure in

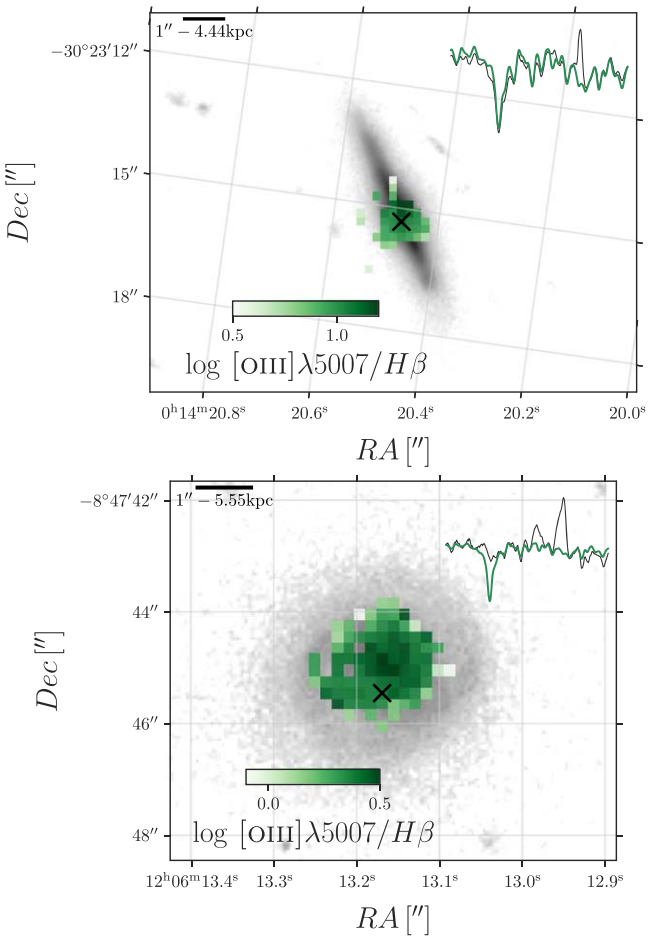

Figure 1. Maps of the [O III]λ5007/Hβ line ratio for two AGN candidates: A2744-07 (top) and MACS 1206–06 (bottom). Only spaxels with S/N > 3 in both [O III]λ5007 and Hβ are included. HST F814W images are shown in grayscale in the background. On the top left, we show the spectrum of a specific spaxel (marked with a dark × in the figure) around the Hβ and [O III] λ5007 lines (4776–5092 Å). The observed spectrum is plotted in black, and the model obtained for the stellar continuum (see sec 3) is shown in green; both spectra are convolved with a 5 pixel box filter for clarity.

timescales shorter than the cluster crossing times, e.g., before or soon after the pericenter passage.

We have included in our sample two objects that show emission lines in the central regions of their stellar disk; these are MACS 1206–06 and A2744-07. We include these objects because we interpret this emission as due to AGN. In Figure 1, we show maps of the [O III]λ5007/Hβ line ratio for these galaxies, including spaxels with a signal-to-noise ratio (S/N) larger than 3 in both emission lines. The emission lines used here and throughout the paper were measured using the HIGHELF code as described in Moretti et al. (2022). In the case of A2744-07 we are also able to measure the Hα and [N II]λ 6584/Hα lines, allowing the full characterization of the central spaxels in a Baldwin–Phillips–Terlevich diagram (Baldwin et al. 1981). Unfortunately, these lines are redshifted out of the MUSE spectral range for MACS 1206–06. In Figure 2 we analyze the central spaxels of these two objects in the [N II]λ 6584/$H\alpha$ versus [O III]λ5007/Hβ BPT diagram. For A2744-07 (blue points), we include spaxels with S/N > 3 in all four lines. Because for MACS 1206–06, we have only information on [O III]λ5007 and Hβ, we can only constrain the y-axis of the diagram. In this case, we plot a horizontal line (purple line) indicating the median [O III]λ5007/Hβ and a band indicating the region between the 10th and 90th percentiles of [O III] λ5007/Hβ in this galaxy, again considering only spaxels with S/N > 3 in the two lines.

All spaxels in A2744-07 that satisfy the S/N criterion lie above the Kewley et al. (2001) line (dotted–dashed line in Figure 2) and can thus be considered ionized by AGNs. The BPT classification for MACS 1206–06 is ambiguous: Not only are we unable to constrain the x-axis, but the y-axis values fall in a region where star formation regions and LINERs (which can be AGNs) coexist. However, because an X-ray point source is detected within the galaxy in the Chandra catalog (Ehlert et al. 2015; Wang et al. 2016) and there is no evidence for current star formation from the spectral synthesis, we conclude that an AGN is the most likely ionization source.

For A2744-01 and SMACS 2131–06 we also identify emission lines, but outside of the stellar disk. This will be discussed in Section 5.1.

3. Spectral Synthesis

In this section we will go into details regarding the spectral synthesis method and the determination of physical parameters for our sample of 21 post-starburst galaxies. The spectral synthesis code is described in Section 3.1, details on the synthesis procedure are presented in Section 3.2, and in Section 3.3 we present the definition of parameters calculated from the SFHs.

3.1. Spectral Synthesis Code: SINOPSIS

This work is heavily based on results from the spectral synthesis code SImulatiNg OPtical Spectra wIth Stellar populations models (SINOPSIS; Fritz et al. 2007, 2011, 2014, 2017). SINOPSIS performs a nonparametric decomposition of galaxy spectra into a combination of stellar population models. This nonparametric approach allows the code to capture even very complex SFHs (Conroy 2013; Leja et al. 2019, but see also Cid Fernandes et al. 2007).

There are a few design choices that set SINOPSIS apart from other widely used nonparametric synthesis codes. First, unlike codes such as STARLIGHT (Cid Fernandes et al. 2005) and PENALIZED PIXEL-FITTING (PPXF; Cappellari 2017), SINOPSIS does not perform full spectral fitting. Instead, the fitting procedure is performed in a selection of continuum band fluxes and spectral indexes (equivalent widths and D_n4000), which focuses the fitting efforts on parts of the spectrum that are more information rich while also making the code less susceptible to problems regarding sky lines and other observational issues. Another distinct design choice in SINOPSIS is the inclusion of emission features in the fitting of stellar population parameters. The emission lines produced by each stellar population element up to the age of 20 Myr are modeled using CLOUDY (Ferland et al. 2017), allowing us to get better constraints for young components. Finally, SINOPSIS allows for a full treatment of dust attenuation (Charlot & Fall 2000). Each stellar population component can be fitted with an independent value of dust optical depth, although we do not take advantage of this feature in this work because our galaxies do not have young stars and this effect is not prominent.

In particular, including emission lines in the fit is very useful for modeling post-starburst galaxies. Because these galaxies do not have emission lines, this provides clear information to the

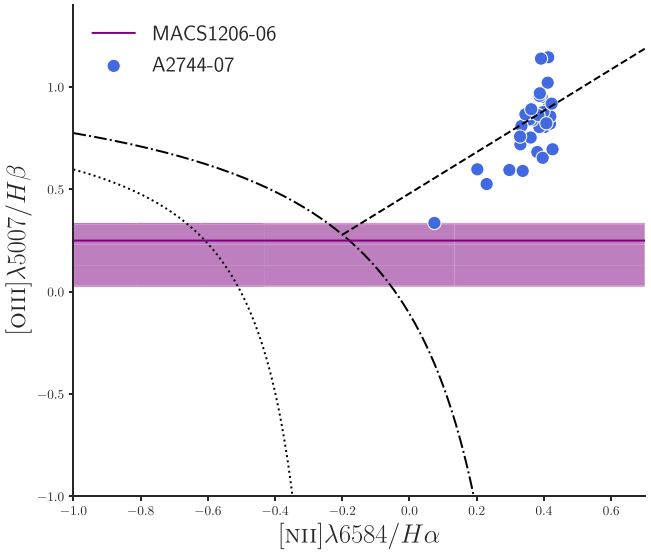

Figure 2. [N II]λ6584/Hα versus [O III]λ5007/Hβ BPT diagram. Blue points are spaxels from A2744-07 with S/N > 3 in all lines in the diagram. The purple horizontal line is the median log [O III]λ5007/Hβ for spaxels in MACS 1206–06 with S/N > 3 in [O III]λ5007 and Hβ; the purple band indicates the region between the 10th and 90th percentiles of [O III]λ5007/Hβ for the same spaxels. For reference, we plot the demarcation lines of Stasińska et al. (2006, dotted line), Kewley et al. (2001, dotted–dashed line), and the transposition of the Kewley et al. (2006) line proposed by Cid Fernandes et al. (2010, dashed line), separating LINERs and Seyferts.

code about the lack of current star formation and prevents solutions that might include small fractions of young stellar populations that are poorly constrained from the optical stellar continuum (see Werle et al. 2019). The fitting of emission lines coupled with the versatility of a nonparametric method makes SINOPSIS the most suitable tool for the current work.

3.2. Synthesis Ingredients and Fitting Procedure

Our spectral synthesis method is based on stellar population spectra from the latest update of the Bruzual & Charlot (2003) models (S. Charlot & G. Bruzual 2022, in preparation). In the optical region, these models rely on the MILES (Sánchez-Blázquez et al. 2006) and IndoUS (Valdes et al. 2004) libraries of stellar spectra, which are combined according to the PARSEC isochrones from Chen et al. (2015) and Bressan et al. (2012). The spectral resolution of the models in the optical (∼2.50Å FWHM) is very similar to the one of MUSE spectra (∼2.55Å FWHM). In this work, we use models generated with a Chabrier (2003) initial mass function. A more detailed description of these models is provided in Werle et al. (2019).

To generate the final set of model spectra used in our fitting procedure, we combined the simple stellar population models from Charlot & Bruzual into 16 age bins from 0 to 10 Gyr[9] and generated composite stellar populations assuming a constant SFR within the bins.

We use three values of metallicity: 0.004, 0.017 (solar), and 0.04. The fitting is done separately for sets of models of different metallicities, and the one with the lowest χ^2 is chosen, i.e., there is no chemical evolution in the derived SFHs.

[9] The limiting ages of the bins are (in years) 0, 1.99×10^6, 3.98×10^6, 6.91×10^6, 1.99×10^7, 5.71×10^7, 2.028×10^8, 5.093×10^8, 8.072×10^8, 1.014×10^9, 1.435×10^9, 2.0×10^9, 3.0×10^9, 4.5×10^9, 6.25×10^9, 8.0×10^9, and 10×10^9.

The effects of dust can be modeled using independent values of extinction with a Cardelli et al. (1989) extinction law. However, because usually higher extinction values affect only stars younger than 20 Myr and these are not identified in our galaxies due to the lack of emission lines, we use one single value of extinction.

In the fits used in this work, we include the equivalent widths of Hα, Hβ, Hδ, and calcium H and K lines, as well as the flux in 32 continuum bands. We note that the features used for each specific galaxy vary according to redshift.

For each of our datacubes, we run SINOPSIS on all spaxels in a contiguous area around the center of the target galaxy where a stellar continuum can be detected; throughout this paper, we refer to these as "valid spaxels." The total number of valid spaxels in all 21 galaxies in our sample is 2230, ranging from 36 for MACS 0257–05 to 318 for MACS 1206–06 with an average of 106 per galaxy. The redshifts for each spaxel, which are required for running SINOPSIS, were determined using PPXF (Cappellari 2017) on Voronoi binned regions with S/N > 5 (as thoroughly described in Moretti et al. 2022). For A2744-05, AS1063SW-01, and SMACS 2131–06, foreground objects were manually masked out.

To obtain the total stellar masses, we sum up the masses obtained with SINOPSIS for all valid spaxels and multiply it by a scale factor so the total mass corresponds to the entire region where the galaxy emission in the MUSE g-band image is 3σ above the background level.

Figure 3 shows examples of SINOPSIS fits for individual spaxels in three post-starburst galaxies in our sample. The examples (A370-04, A370-05, and A2744-02) were chosen to illustrate different levels of post-starburst features.

3.3. Star Formation History Feature Extraction

To interpret the 2230 derived SFHs (one for each valid spaxel), we chose to reduce their dimensionality by extracting two relevant features: (i) the time since quenching (t_Q), and (ii) the fraction of stellar mass formed in the past 1.5 Gyr ($\mu_{1.5}$).

We define the time since quenching t_Q as the time elapsed since the moment when the galaxy reaches 98% of the total mass ever assembled, i.e., counting also stars that have already died. This parameter is calculated from a cumulative SFH obtained by converting the SFR of each age bin to mass fractions, summing the mass fractions cumulatively from the oldest to the youngest, and linearly interpolating between points. We then find the age where the mass fraction is 98%. We choose not to use the 100% mass fraction to avoid the influence of possible tiny insignificant fluctuations in the SFR. The value of 98% is close enough to 100% to give a robust definition of quenching without being affected by these fluctuations.

From the same cumulative SFHs, we calculate the fraction of stellar mass assembled in the past 1.5 Gyr ($\mu_{1.5}$). The same quantity was also explored by Pawlik et al. (2018) and Wild et al. (2020). Although 1 Gyr would be closer to the lifetime of A-type stars that characterize the spectra of post-starburst galaxies, there can be an SFR enhancement starting slightly before that time. Thus, we chose the 1.5 Gyr limit as it includes the whole timescale over which the SFR may have been enhanced. Nevertheless, the mass fractions calculated using 1 or 1.5 Gyr are very similar, and this choice does not affect our results. Note that here and throughout the paper we are not using strict terminology when saying "in the past 1.5 Gyr" or

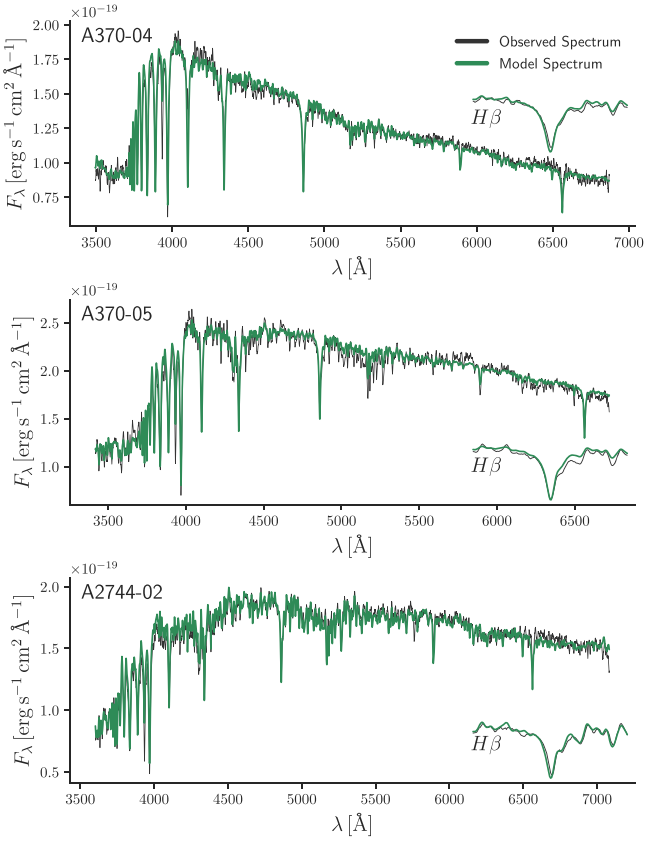

Figure 3. Three examples of SINOPSIS fits for post-starburst galaxies in our sample. Panels show integrated observed (gray) and model (green) spectra for (top to bottom) A370-04, A370-05, and A2744-02. Spectra are convolved with a 5 pixel box filter to improve visualization. We include a zoom-in to the spectral region around the Hβ line (4861 $\pm$ 75 Å).

"time since quenching" as we are referring to lookback times that have as reference the age of the universe in the galaxy redshift, and not at $z = 0$ as would be implied by taking these sentences literally.

4. Star Formation Histories

We now focus on the SFHs derived by SINOPSIS. In Section 4.1 we show the integrated SFHs of all galaxies; we then look at the distributions and maps of t_Q and $\mu_{1.5}$ (Sections 4.2 and 4.3, respectively) and present our interpretation of the general trends in Section 4.4.

4.1. Integrated Star Formation Histories

The definition of post-starburst is purely empirical and can accommodate a variety of SFHs. The lack of emission lines implies that SFR($t < 20$Myr) = 0, and the strong Balmer absorption lines indicate the presence of A-type stars whose lifetime is $\sim$1 Gyr. This constrains the galaxies to SFHs that were rapidly quenched in $t < 1$ Gyr but does not indicate if the SFR was actually enhanced before quenching (i.e., if there was a burst) or if the SFR suddenly dropped sometime in the past 1 Gyr without any prior enhancement. To examine this, we have calculated the median of the spaxel-by-spaxel SFHs for each galaxy, as shown in Figure 4. Median SFHs are plotted in blue, with shaded regions indicating the interquartile regions (between the 25th and 75th percentiles); a dashed line indicates a lookback time of 1.5 Gyr. Note that we choose to represent the SFHs as SFR versus log t to highlight the bursts, but we should keep in mind that older bins are much wider, and thus low SFRs at old ages can still correspond to a very large fraction of mass formed.

For most galaxies (16 out of 21), it is possible to identify a clear and isolated burst of star formation prior to quenching, and in some cases, this burst is the main feature in the SFH. In other cases, the SFHs are more complex and it is hard to identify a single burst. In the case of A2744-02, A2744-07, and SMACS 2031–02 (panels b, d, and p) there seems to be an enhancement in SFR close to the 1.5 Gyr mark followed by a smaller enhancement in more recent times. For A2744-08 (panel e), there is a strong drop in the SFR at around 1.5 Gyr ago after which SFR is sustained at an almost constant level until quenched. In the case of MACS 0257–05 (panel n) there seems to be a burst 1.5 Gyr ago but the feature is unclear as the SFR was rising prior to that event.

Notwithstanding these peculiarities, all of these SFHs can be described as rapidly quenched, as all of them display a sharp decrease in the SFR at $t < 1$ Gyr. Although in some cases (e.g., A2744-07, A2744-08, MACS 0257–04, and SMACS 2131–05; panels d, e, m, and q) some residual star formation is sustained after the main quenching event. This residual star formation is associated with very small mass fractions that do not count toward our definition of quenched. That being said, it is important to have this effect in mind when analyzing the results for these galaxies.

In most cases, the interquartile regions traced by the shaded bands in Figure 4 do not deviate from the median shape of the SFH, indicating that the SFH is somewhat similar across the spaxels of a single galaxy. Indeed, galaxies in our sample are generally post-starburst in all spaxels. Only 3.5% of the spaxels for which Hδ_A can be measured (91% of the spaxels in our sample) have H$\delta_A < 3$ Å, the typical threshold to define a spectrum as quiescent.

4.2. Distributions of t_Q and $\mu_{1.5}$

In Figure 5, we show box plots tracing the distributions of t_Q (top panel) and $\mu_{1.5}$ (bottom panel). Boxes indicate the interquartile regions with horizontal lines within the boxes showing the median value. Dark lines outside the boxes extend from the 15th to the 85th percentiles.

The median values of t_Q vary from 65 Myr for A2744-01 to 621 Myr for SMACS 2131–05, with some spaxels reaching times older than 800 Myr. The spaxel-by-spaxel mean value for the entire sample is 327 Myr with a standard deviation of 250 Myr.

As for $\mu_{1.5}$, median values go from 7.7% for SMACS 2131–05 to 52.3% for MACS 0257–03, with some spaxel-by-spaxel values reaching more than 60%. Keeping in mind that 1.5 Gyr corresponds only to 15%–17% of the time over which these galaxies could form stars (from the big bang to the age of the universe at the redshift of observation) and considering that generally the SFR declines with time in normal galaxies, it is noteworthy that the majority of our galaxies have median $\mu_{1.5}$ values greater than 15%. The average $\mu_{1.5}$ over all spaxels is 26.10% with a standard deviation of 14.15%. We note that the median values obtained for $\mu_{1.5}$ are generally in the same range as previous works based on integrated spectra (e.g., Pawlik et al. 2018; Wild et al. 2020), which is noteworthy considering the different population synthesis methods and post-starburst selection criteria.

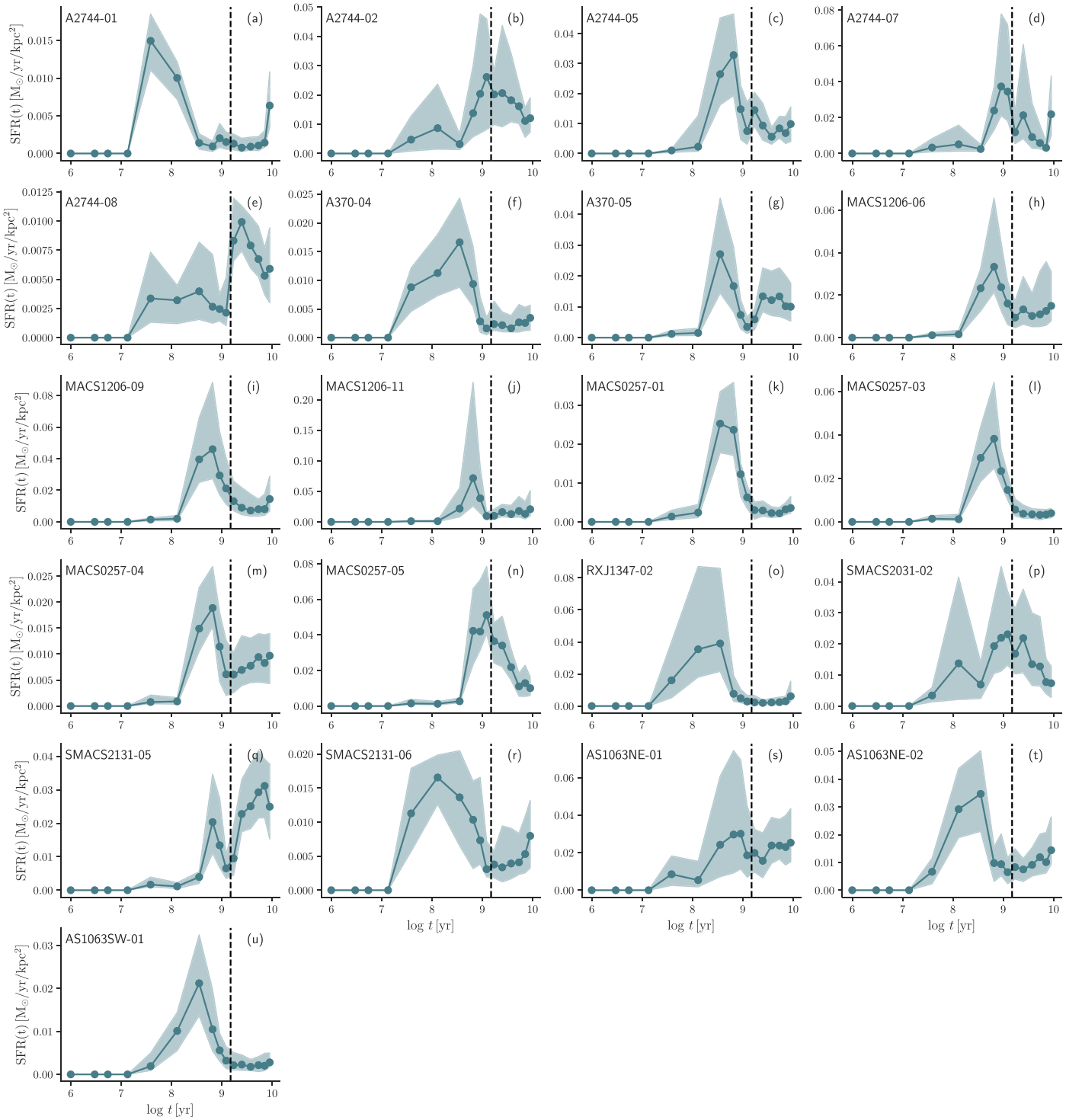

Figure 4. Median SFHs for galaxies in our sample, with shaded bands indicating the interquartile regions. Points are plotted at the central lookback time of each age bin. Dashed vertical lines indicate the reference lookback time of 1.5 Gyr.

4.3. Quenching Directions

We now proceed to a spatially resolved analysis of the SINOPSIS results. In Figure 6 we show maps of t_Q for the 12 biggest (in apparent size) galaxies in our sample, for which the datacubes have more than 70 valid spaxels (see definition in Section 3.2). Darker colors indicate older t_Q, and the limits of the color bars are set to the 20th and 80th percentiles of t_Q in each galaxy. The variation of t_Q within each galaxy (Δt_Q) is annotated in each panel; this parameter is an estimate of how quickly the quenching happened. To ensure a robust estimation and prevent eventual outlier spaxels from biasing our results, we define Δt_Q as the difference between the 90th and 10th percentiles of t_Q instead of as the difference between the maximum and minimum values.

The maps in Figure 6 indicate a diversity of quenching patterns. For 4 out of 12 galaxies the quenching clearly happened first in the outskirts. This is the case for A2744-02, MACS 0257–04, SMACS 2031–02, and AS1063NE-01

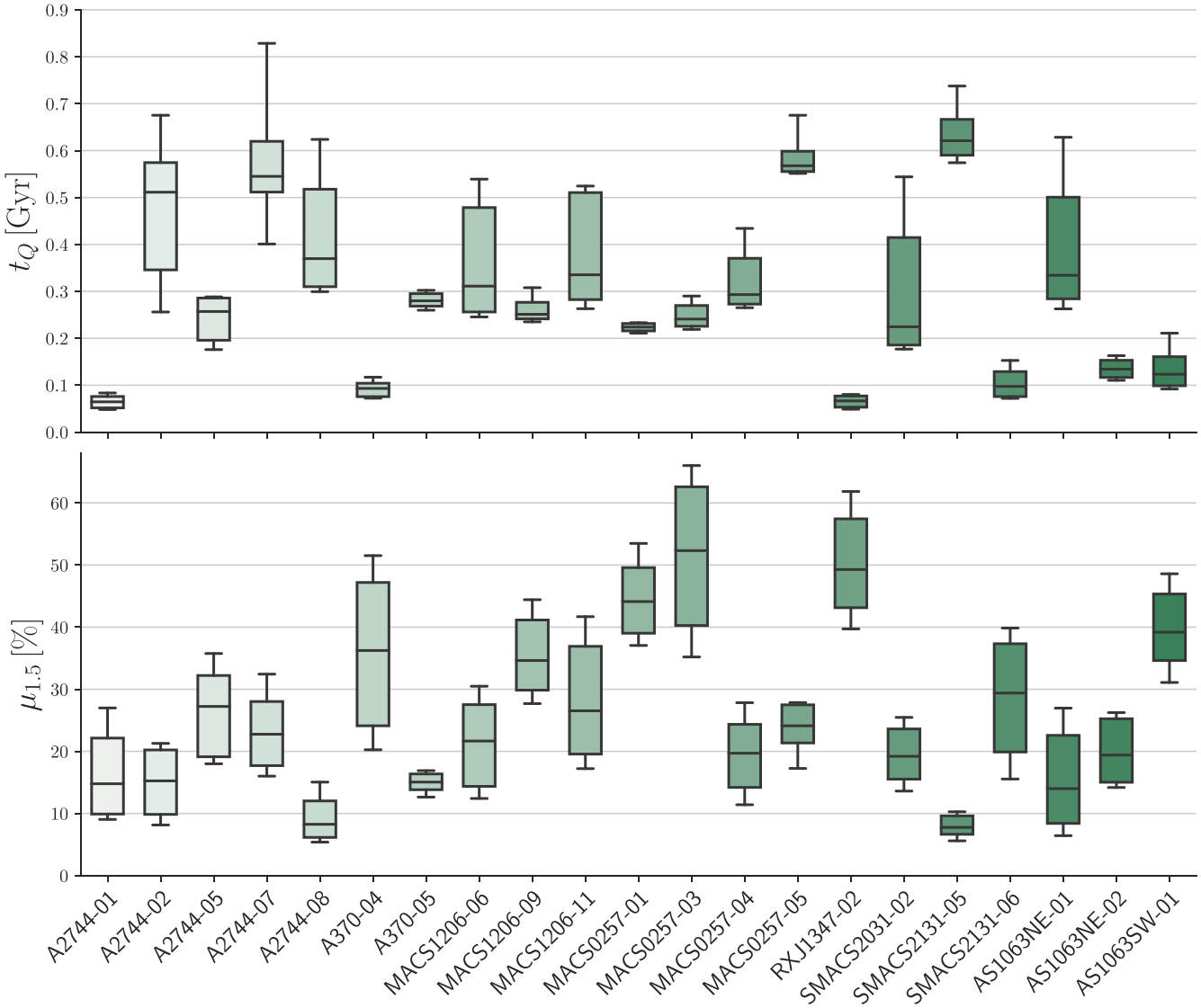

Figure 5. Box plots tracing the distributions of time since quenching (t_Q, top) and the fraction of the mass assembled in the past 1.5 Gyr ($\mu_{1.5}$, bottom). Boxes in shades of green indicate the regions between the 25th and 75th percentiles (interquartile regions), horizontal lines within the boxes indicate the median, and whiskers (dark lines outside the boxes) indicate the extent between the 15th and 85th percentiles. The color scale is only to improve readability and does not indicate any physical quantity.

(panels a, h, j, and k). This outside-in pattern is reminiscent of the truncated gas disks observed in galaxies undergoing ram pressure stripping (e.g., Gullieuszik et al. 2017; Poggianti et al. 2019). We note that D'Eugenio et al. (2020) also find centrally concentrated starbursts in post-starbursts in environments that are not prone to ram pressure, where this stellar population gradient is attributed to mergers. However, as we will show in Figure 13, the stellar kinematics maps of our galaxies are very regular and inconsistent with the merger hypothesis.

For A370-04, A370-05, MACS 1206–11, RX J1347–02, and AS1063NE-02 (panels c, d, g, i, and l) the t_Q distribution is less clear, following a side-to-side or irregular pattern that is also consistent with ram pressure stripping. The low dynamic range of t_Q in these galaxies (except for MACS 1206–11 in panel g) points to a very fast quenching process, uniform over the whole galaxy.

For three galaxies (A2744-07, MACS 1206–06, and MACS 1206–09, panels b, e, and f), the t_Q maps indicate an inside-out quenching, which is consistent with the stellar population gradients of the general population of star-forming galaxies (older in the center). In the cases of A2744-07 and MACS 1206–06, we find indication of AGN emission in the central region of the stellar disks (see Section 2.2).

For MACS 1206–09, despite the general inside-out pattern, we do see that the outer parts of the disk quenched slightly earlier, pointing to a combination of inside out and outside in. This pattern could be interpreted as the combination of inside-out quenching due to AGN and outside-in quenching due to ram pressure, as found by George et al. (2019). We note that this pattern should not be interpreted as peculiar, as there is evidence in the literature for an enhanced AGN fraction among galaxies undergoing ram pressure stripping (e.g., Poggianti et al. 2017; Ricarte et al. 2020; Peluso et al. 2022), although this is still debated (see Roman-Oliveira et al. 2019; Boselli et al. 2021) Despite this duality, we choose to define this galaxy as quenched from the inside out as this is the most conspicuous pattern.

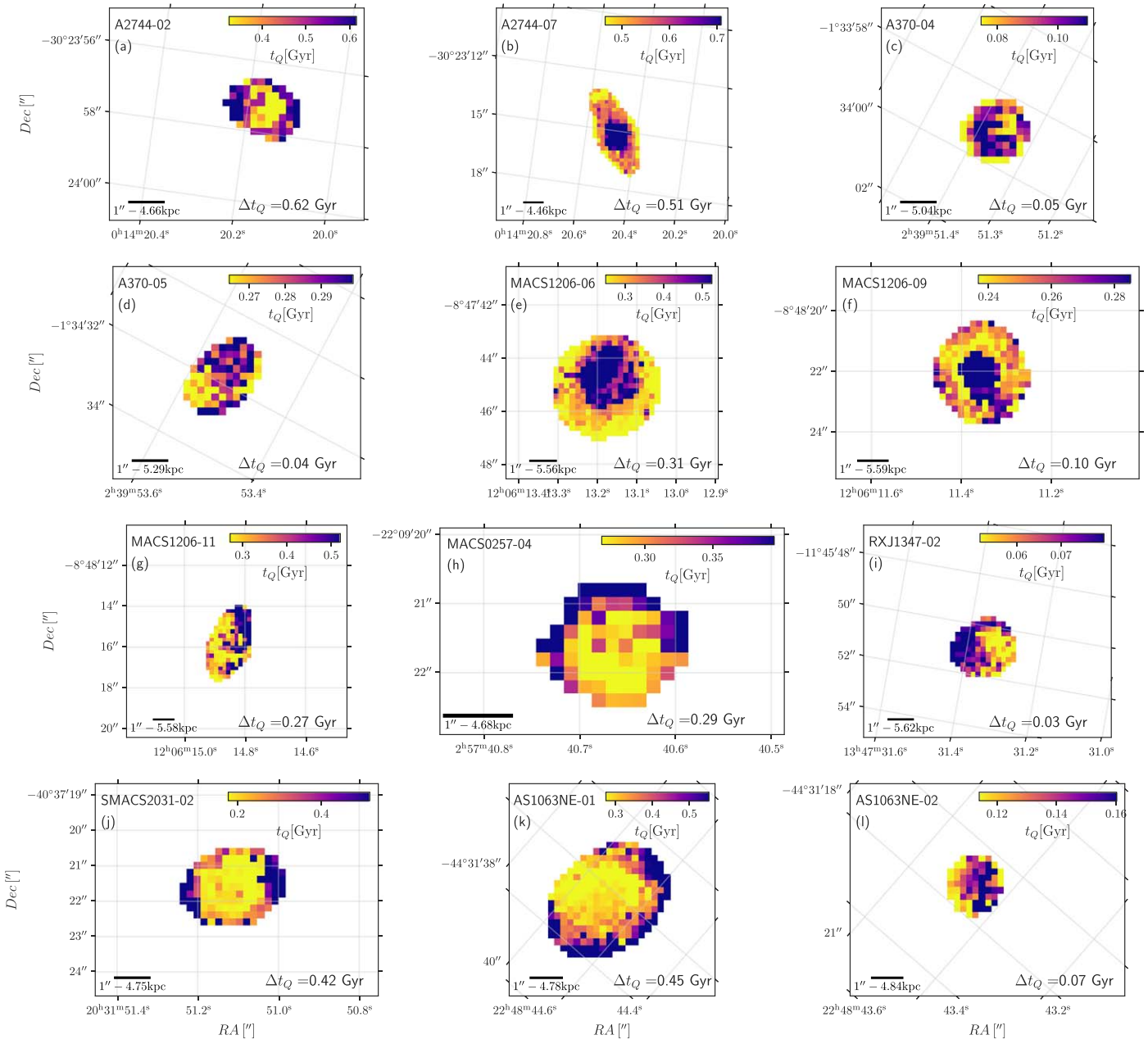

Figure 6. Maps of quenching time (t_Q) for all cubes with more than 70 valid spaxels and no foreground objects. Darker colors indicate spaxels quenched at older lookback times. Minimum and maximum values of the color bars are set to the 20th and 80th percentiles of each t_Q map. Δt_Q values are annotated in each panel.

The maps of $\mu_{1.5}$ for the same 12 galaxies are shown in Figure 7. To improve visualization we saturate the color scales in the 20th and 80th percentiles of $\mu_{1.5}$ in each galaxy. In most cases, the $\mu_{1.5}$ maps follow trends that are similar to what we see for t_Q. For the galaxies that show an outside-in pattern in the t_Q maps (A2744-02, MACS 0257–04, SMACS 2031–02, and AS1063NE-01), the same trend is clearly reproduced for 3/4. In the case of SMACS 2031–02 (panel j), the $\mu_{1.5}$ morphology is slightly more complex, as the central region of this galaxy has low mass fractions. This can be understood as the central regions of the galaxy being more gas poor prior to the quenching event and thus not assembling large mass fractions during the burst. On the other hand, MACS 1206–11 shows a clear outside-in pattern in the $\mu_{1.5}$ map, while the t_Q map is less clear, showing something between a side-to-side and an outside-in pattern. In this case, we understand that it is safer to classify the galaxy as quenched from the outside in because $\mu_{1.5}$ is a more robust parameter and the Δt_Q of this galaxy is larger than the typical value associated with side-to-side/irregular quenching patterns.

4.4. Putting the Pieces Together

So far, we have presented results on a case-by-case basis, which is necessary due to the diversity of quenching histories in our sample. However, within this diversity lies a general trend. In Figure 8, we plot log stellar mass against Δt_Q, coloring galaxies according to the direction of their quenching maps. Besides the galaxies already shown in Figures 6 and 7, we also include classifications for other five galaxies that are not among the biggest (fewer than 70 valid spaxels) but still display clear patterns: These are A2744-01, MACS 0257–01,

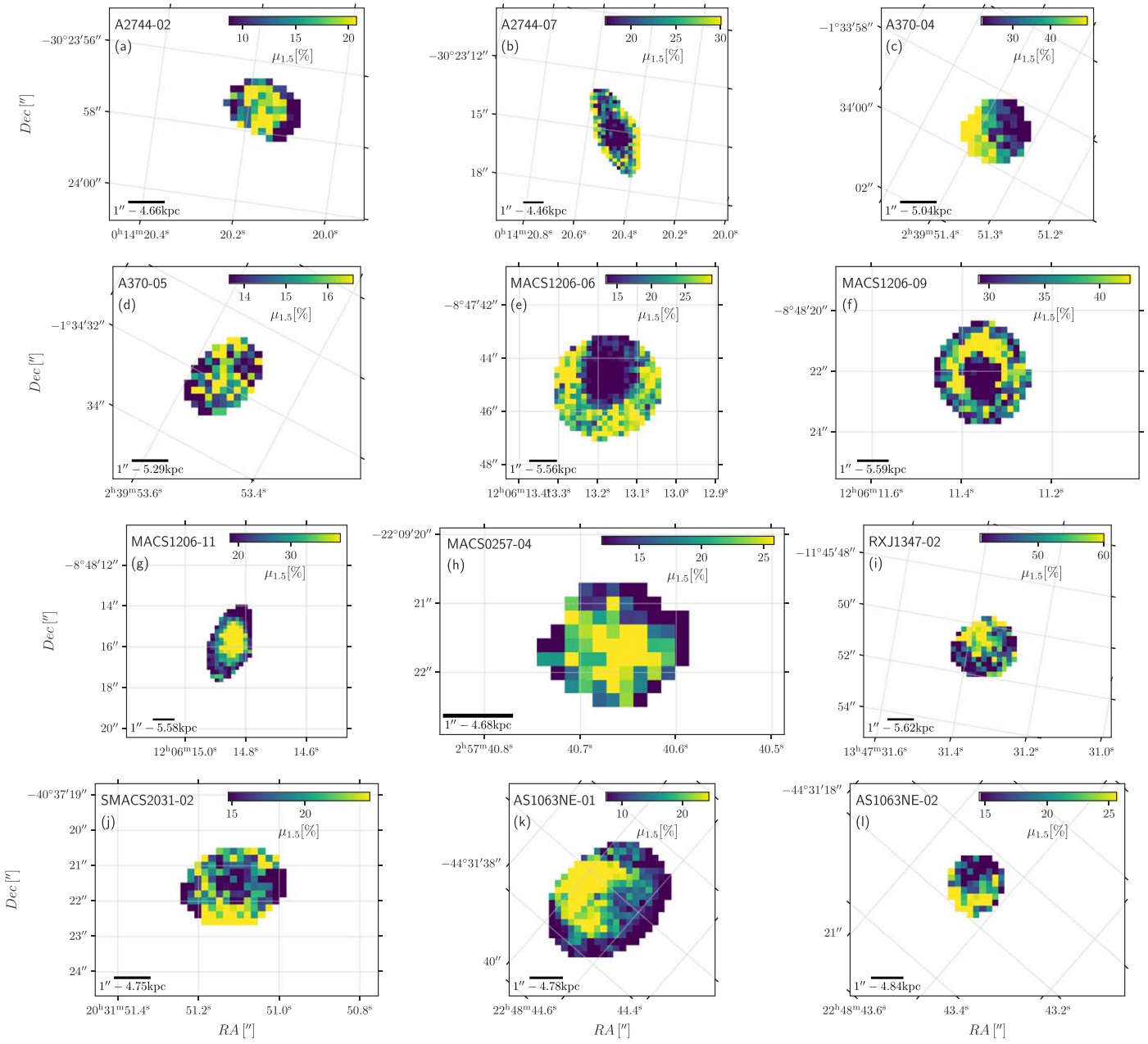

Figure 7. Maps of the fraction of mass assembled in the past 1.5 Gyr ($\mu_{1.5}$) for all cubes with more than 70 valid spaxels and no foreground objects. Minimum and maximum values of the color bars are set to the 20th and 80th percentiles of each map.

MACS 0257–03, MACS 0257–05, and SMACS 2131–05. We still omit galaxies where part of the stellar disk is obscured by a foreground object, which can affect the observed quenching patterns and render them unclear.

Figure 8 shows that (i) all of the side-to-side/irregular quenching patterns are in low-mass galaxies ($\log M/M_{\odot} < 10.5$), and (ii) all of the inside-out patterns are more massive galaxies. For the low-mass end, we observe generally lower Δt_Q (fast quenching) with either a side-to-side pattern or an irregular/unclear morphology in the t_Q and $\mu_{1.5}$ maps. Our interpretation, based on the classical Gunn et al. (1972) model, is that the anchoring force that binds the gas to the stellar disk is generally lower, making it easier for ram pressure to quickly remove the gas. In more massive galaxies, we expect AGNs to be more common (Kauffmann et al. 2003; Lopes et al. 2017; Sánchez et al. 2018) and stellar population gradients to more strongly affect the evolution of the galaxy before entering the cluster. Indeed, for high-mass galaxies, we observe some inside-out patterns left by their previous evolution in a low-density environment and/or AGN-induced quenching. Note that this does not mean that the effects of ram pressure should be completely discarded for these galaxies, just that their stellar population gradients are more strongly shaped by other processes. In fact, as stated before, for MACS 1206–09 the maps point to a combination of secular growth and ram pressure, as both the inner regions and the outskirts have older t_Q and lower $\mu_{1.5}$.

The stellar-mass range is unconstrained for galaxies displaying outside-in quenching patterns. These seem to be objects that, while affected by ram pressure, are able to better retain their gas, leading to a longer global timescale for stripping of the gas (longer Δt_Q). Because the stellar-mass

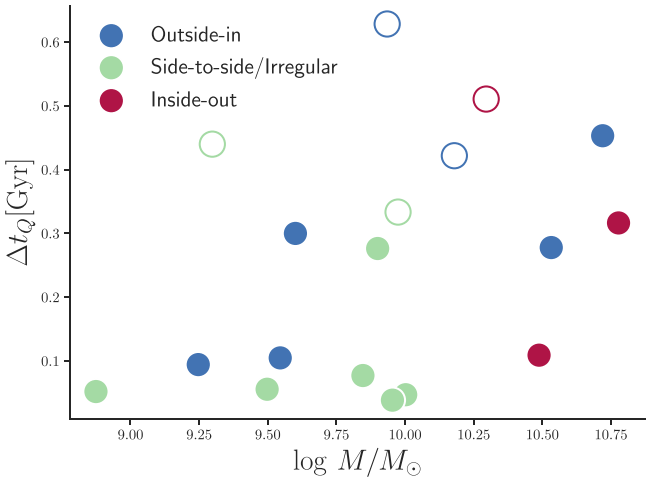

Figure 8. Log stellar mass ($\log M/M_\odot$) vs. the variation of t_Q within each galaxy (Δt_Q). Colors indicate the quenching direction measured from the $\mu_{1.5}$ and t_Q maps. Galaxies without a clear enhancement of SFR prior to quenching are shown as open circles.

surface density is lower in the outskirts, these regions are stripped first and the starburst is centrally concentrated, ultimately leading to the outside-in gradients that we observe.

Galaxies lacking a clear enhancement of SFR prior to quenching (as seen in their integrated SFHs; Figure 4) are shown as open circles in Figure 8. These objects have typically large Δt_Q (>300 Myr) regardless of the quenching direction. These longer timescales can be interpreted as an indication that the lack of a burst is not related to how much gas was initially available for star formation, but to other factors (e.g., more circular orbits within the cluster, feedback, etc.) that lead to the slow (when compared to other post-starbursts) conversion of this gas into stars.

In addition to what was previously discussed, Figure 8 also shows that there is a certain relation between $\log M/M_\odot$ and Δt_Q. In particular, it is interesting to see this relation for galaxies displaying an outside-in quenching pattern: Although these are observed in a wide range of masses, the quenching seems to happen faster at lower masses. We note that, although our sample is large enough so we can identify a variety of objects, it is too small to allow us to reliably study statistical trends, and larger samples will be required to confirm this interpretation.

5. Special Cases

Some objects in our sample have particularly interesting features revealed by the analysis of their emission-line maps. In this section, we deviate from the main thread of the paper to concentrate on those cases. In Section 5.1 we showcase two objects with tails of ionized gas, and in Section 5.2 we take a closer look at the emission-line properties of A2744-07.

5.1. Tails of Ionized Gas

We have identified two post-starbursts that, although lacking any emission lines in their stellar disks, display long tails of ionized gas; these are A2744-01 and SMACS 2131–06. We note that for A2744-01 these tails have already been identified by Owers et al. (2012) and Moretti et al. (2022). This intriguing feature is shown in Figure 9, where we plot HST F814W images of these two objects with the [O II]λ3727 flux in red.

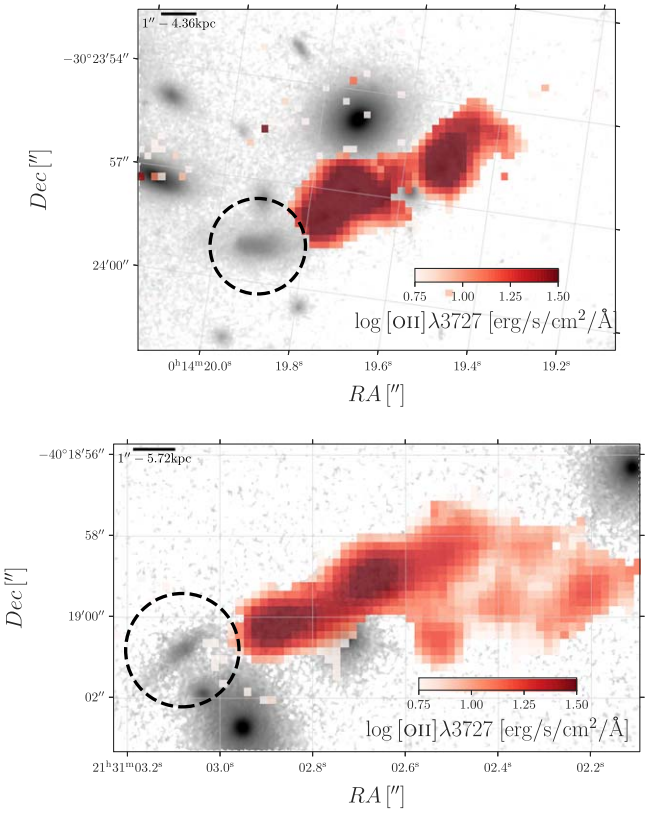

Figure 9. HST F814W images (gray) of A2744-01 (top) and SMACS 2131–06 (bottom) with [O II]λ3727 flux (in erg/s/cm^2) measured from the MUSE datacubes shown in red. The position of the galaxies is marked by dashed circles of arbitrary radius centered in the HST coordinates of each galaxy.

These tails can be interpreted as the smoking gun of ram pressure stripping, setting these objects as missing links between post-starbursts and jellyfish galaxies.

The case of A2744-01 is particularly interesting. In Figure 10, we plot the map of $\mu_{1.5}$ for this galaxy (yellow to blue color map) and the flux map in of the [O II]λ3727 line (red color map). The $\mu_{1.5}$ map has a side-to-side gradient that is aligned with the tail of ionized gas in such a way that spaxels closer to the tail have larger fractions of young stellar populations (more prominent bursts). Unfortunately, we are unable to do the same analysis for SMACS 2131–06, as in the MUSE datacube it is strongly blended with a foreground object in the south, which prevents us from reliably probing the stellar population gradient.

Other properties of A2744-01 are also worth mentioning. Of all galaxies in our sample, it is the one with the lowest mass ($\log M_\star/M_\odot = 8.9$), lowest median t_Q (64 Myr; see Figure 5), and a very low Δt_Q of 51 Myr. It also has very strong features with a blue spectrum (see top panel of Figure 3), integrated Hδ_A of 6.78 Å, and a very clear recent burst in the SFH (see the first panel in Figure 4). Its median $\mu_{1.5}$ is 14.78%.

5.2. The Case of A2744-07

Another object with peculiar emission-line features is A2744-07. In Figure 11 we show the [O II]λ3727 flux (top) and velocity (bottom) for this object.

Besides the AGN in the central region (see Section 2.2), two strips of gas can be seen in the map, one to the northeast, extending ~20 kpc along and beyond the stellar disk, and one

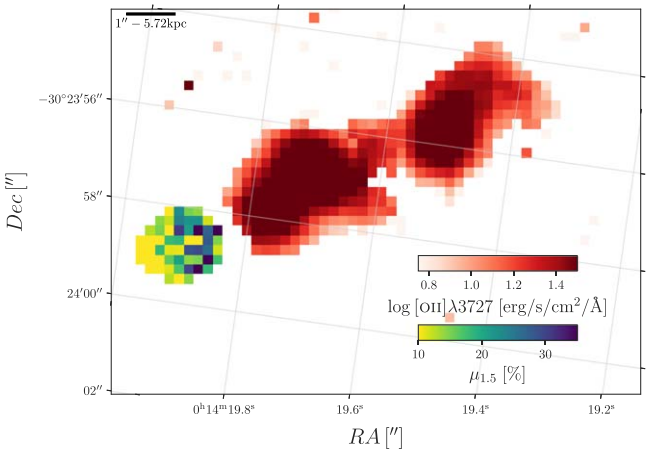

Figure 10. Maps of $\mu_{1.5}$ (yellow to blue color map) and [O II]λ3727 flux (red color map) for the galaxy A2744-01.

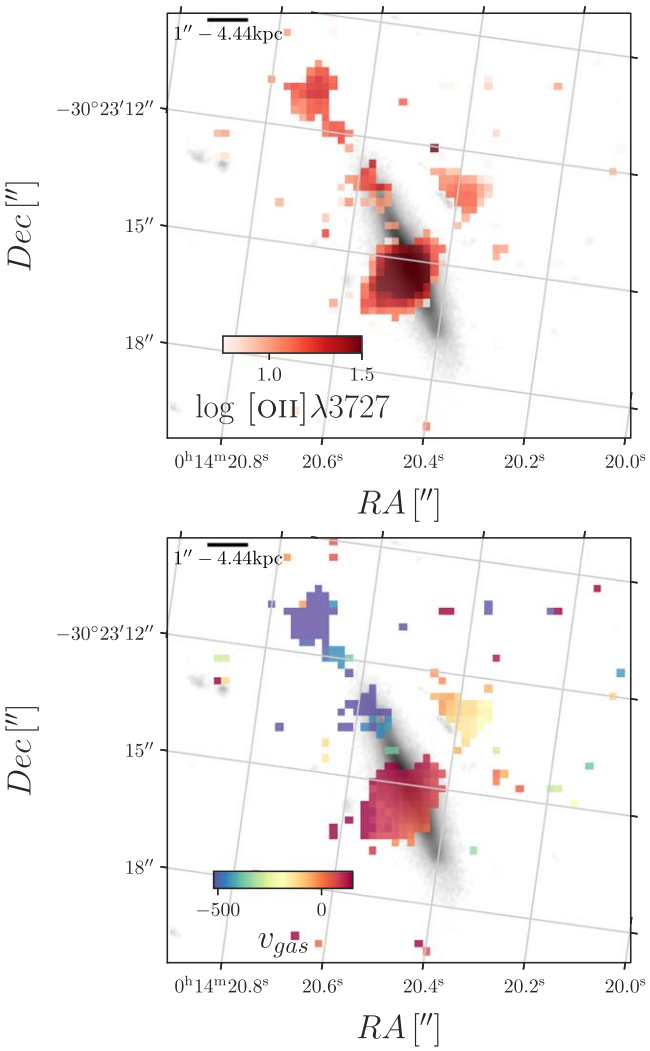

Figure 11. MUSE [O II]λ3727 map for all spaxels where the line is detected with S/N > 3 (top panel) and [O II]λ3727 velocity field (bottom panel) for the galaxy A2744-07. The HST F814W image is shown in grayscale in the background.

to the east, extending ∼12 kpc perpendicular to the stellar disk. In addition to [O II]λ3727, these features are also visible in Hα, but not in [O III]λ5007, which points to a soft-ionization

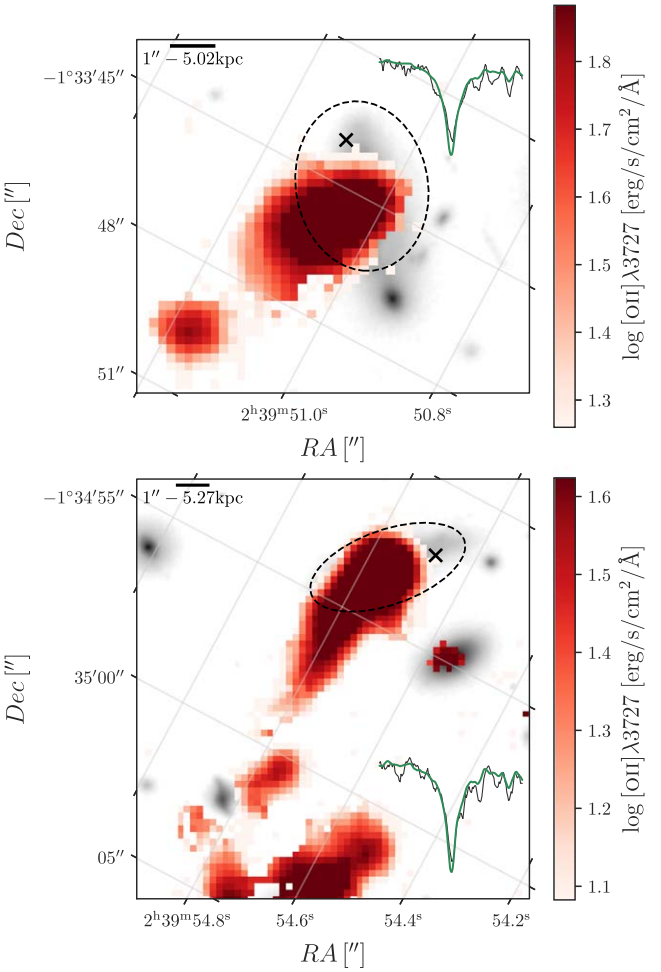

Figure 12. [O II]λ3727 flux map of two jellyfish galaxies from Moretti et al. (2022), A370-06 in the top and A370-08 in the bottom, with dashed ellipses showing the extension of the stellar disk. A dark "×" marks the position of a spaxel that has recently been stripped of gas; the model (green) and observed (black) spectra of these spaxels in a 75 Å window centered on the Hβ line are plotted on the right-hand side. The HST F814W image is shown in grayscale in the background.

source, although the strips seem to be spatially correlated with the central AGN. Both gas strips are blueshifted with respect to the central region (bottom panel of Figure 11); in the case of the northern strip, the velocities reach up to ∼−500 km s^{-1}.

We are unable to determine if these features are caused by the AGN, by ram pressure, or (most likely) a complex combination of the two. Given that ram pressure stripping is known to trigger (or maybe be helped by) an AGN (e.g., Poggianti et al. 2017; Ricarte et al. 2020), we should expect some transition objects such as A2744-07 to display features of both AGN and ram pressure.

6. Further Clues on Ram Pressure Stripping

Our results so far indicate that ram pressure stripping is the main driver of fast quenching in the centers of clusters at intermediate redshift. This hypothesis is strengthened by several results in the literature that also point to ram pressure as the most common path to the post-starburst phase in dense environments (Poggianti et al. 2004, 2009; Vulcani et al. 2020). In this work, the main evidence for this comes from the direction of the quenching traced by t_Q and $\mu_{1.5}$, as these maps

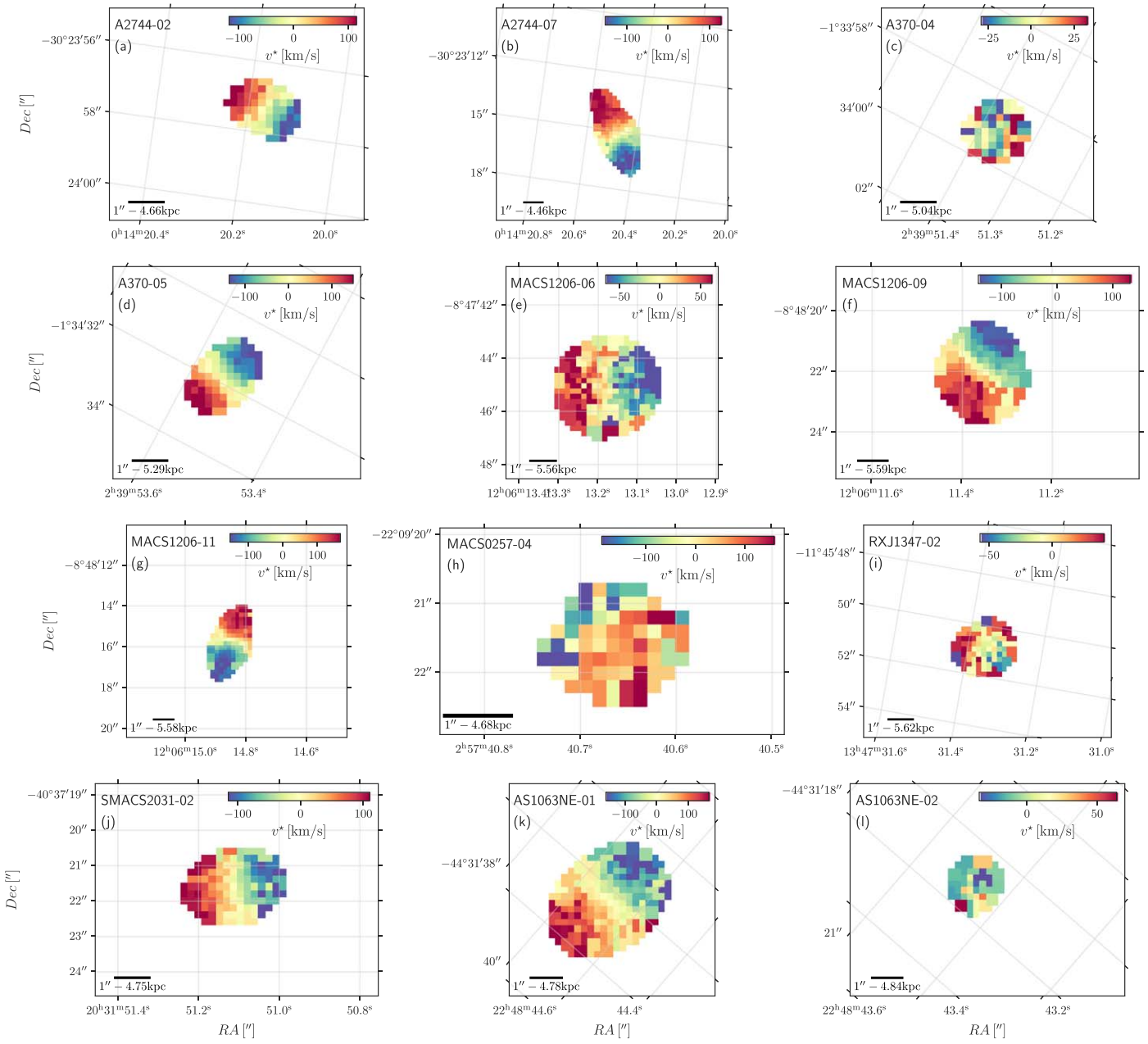

Figure 13. Stellar velocity ($v^\star$) maps derived with PPXF for the same 12 galaxies shown in Figures 6 and 7.

show that most galaxies are quenched from the outside in or display a side-to-side/irregular stellar population gradient. Both features are consistent with the stripping of gas via ram pressure. Inside-out quenching patterns expected from AGN-driven quenching are observed only in three galaxies, all of which are on the high-mass end of the distribution for our sample.

Complementary evidence comes from two special cases (shown in Figure 9) for which we find tails of ionized gas, indicating that the gas was very recently stripped. This connection between post-starburst and jellyfish galaxies can also be explored from the other way around, i.e., identifying post-starburst features in galaxies undergoing ram pressure stripping, as done by Gullieuszik et al. (2017) and Poggianti et al. (2019) for jellyfish galaxies in the local universe. Thus, it is natural to attempt the same analysis for stripped galaxies in the same clusters from which we selected our sample of post-starbursts. In Figure 12 we show maps of [O II]λ3727 flux from two jellyfish galaxies from the Moretti et al. (2022) sample, A370-06 on the top panel and A370-08 on the bottom panel. Dashed ellipses in each panel indicate the extent of the stellar disk. For each of these galaxies, we choose a spaxel that has already been stripped of gas (marked with a dark "×") and plot the corresponding spectra around the Hβ line. The spectra in these stripped regions show strong Hβ absorption lines, and the same happens for other Balmer lines, indicating that these objects are likely to be the progenitors of post-starburst galaxies.

A crucial piece of information for confirming ram pressure stripping is the stellar velocity field of a galaxy (e.g., Vulcani et al. 2020). Disturbed stellar kinematics can be associated with gravitational interactions or mergers, while ram pressure affects only the gas and leaves the stellar kinematics unperturbed. Unfortunately, at this redshift, due to the spatial resolution and

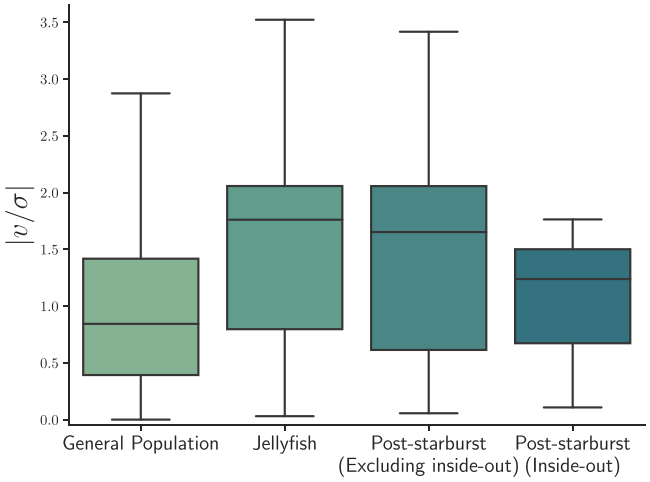

Figure 14. Box plots tracing the absolute value of v/σ for (from left to right) the general population of cluster galaxies, jellyfish galaxies from the same clusters, post-starbursts not including the ones with inside-out quenching, and post-starbursts with inside-out quenching. Boxes are between the interquartile regions, horizontal lines within the boxes indicate the median, and whiskers extend out to 1.5 times the interquartile regions.

S/N, it is not possible to establish if an irregular velocity map corresponds to actually disturbed stellar kinematics or just noise. Therefore, irregular kinematic maps should be interpreted as ambiguous. However, it is possible to confirm when the kinematics is globally regular.

Stellar velocity fields derived with PPXF for the same 12 galaxies of Figures 6 and 7 are shown in Figure 13. The stellar kinematics is usually very regular. Exceptions are A370-04, AS1063NE-02, and RX J1347–02, all of which are faint and have small apparent size, for which the velocity maps are not reliable. Thus, the kinematical maps for these galaxies are very uncertain. We interpret these regular kinematical maps as complementary evidence that ram pressure is the main driver of fast quenching in our sample.

Another relevant piece of the puzzle is the galaxy environment. To probe this, we calculate the absolute value of the peculiar velocity of each galaxy relative to the cluster redshift, normalized by the cluster velocity dispersion ($|v/\sigma|$). The value of $|v/\sigma|$ gives us an indication of the infall stage of each galaxy. Objects with higher $|v/\sigma|$ are more likely to be rapidly infalling and experiencing ram pressure stripping, while objects with lower $|v/\sigma|$ are generally more likely to be relaxed.

Box plots tracing the distributions of $|v/\sigma|$ for different galaxy classes are shown in Figure 14. We divide the post-starburst population (marked PSB in the figure) into two subclasses: the ones with outside-in or side-by-side/irregular quenching patterns and the ones with inside-out quenching patterns. Note that in the case of inside-out quenched post-starbursts, the box plot is produced with only three galaxies, and the $|v/\sigma|$ values for these galaxies correspond to the median and to the extremes of the whiskers in the box plot.

The box plots in Figure 14 show that post-starbursts with outside-in or side-to-side/irregular quenching patterns have a $|v/\sigma|$ distribution similar to those of jellyfish galaxies, while post-starbursts with inside-out quenching patterns are closer to the general population of cluster galaxies. This serves as further evidence that post-starbursts with outside-in or side-to-side/irregular quenching patterns had their gas removed by ram pressure stripping, while inside-out quenching patterns may be related also to other processes such as AGN feedback.

7. Conclusions

In this work, we have presented results from the analysis of MUSE integral field spectroscopy of 21 post-starburst galaxies in the centers of eight clusters at $z \sim 0.3$–0.4.

We used the SINOPSIS spectral synthesis code to retrieve spatially resolved SFHs of all 21 objects, finding a clear enhancement in SFR prior to quenching in 16 cases. From these, we calculate the time since quenching (t_Q) and the fraction of stellar mass assembled in the past 1.5 Gyr ($\mu_1.5$).

We find that most galaxies in our sample have quenched their star formation from the outside in (seven objects) or show a side-to-side/irregular pattern (eight objects). Only three objects show an inside-out quenching pattern, all of which are at the high-mass end of our sample. For two of them, the quenching can be associated with an AGN. For three objects the quenching direction is unclear. The variation in quenching times within each galaxy (Δt_Q) correlates (although weakly) with the galaxy mass, in the sense that less massive galaxies are more rapidly quenched.

For two objects in our sample, we identify tails of ionized gas showing that these galaxies are caught in a transition from jellyfish to post-starburst. In the case of A2744-01, we are able to identify a stellar population gradient in the direction of the tail: Spaxels closer to the tail have assembled higher fractions of stellar mass in the recent past.

We have shown that the stellar kinematics of galaxies in our sample is generally regular. Also, post-starbursts displaying an outside-in or a side-to-side/irregular quenching pattern have a distribution of absolute velocities within the cluster similar to that of galaxies currently undergoing ram pressure stripping. On the other hand, for the three galaxies for which we identify an inside-out quenching pattern, the velocities within the cluster are closer to the ones of the general population of cluster galaxies.

As a whole, our results point to ram pressure stripping as the main driver of fast quenching in dense environments at intermediate redshift, with AGNs being relevant only for galaxies of high stellar mass ($\log M/M_\odot > 10.5$).

A.W. thanks Catarina Aydar and Daniel Ruschel Dutra for important discussions about this work, and Abilio Mateus for providing a first contact with post-starburst galaxies. We thank the anonymous referee for suggestions that have improved the paper. This project has received funding from the European Research Council (ERC) under the European Union's Horizon 2020 research and innovation program (grant agreement No. 833824, GASP project). B.V. and M.G. also acknowledge the Italian PRIN-Miur 2017 (PI A. Cimatti). We acknowledge funding from the INAF main-stream funding program (PI B. Vulcani). J.F. acknowledges financial support from the UNAM- DGAPA-PAPIIT IN111620 grant, México. G.B. acknowledges financial support from the National Autonomous University of Mexico (UNAM) through grant No. DGAPA/PAPIIT BG100622.

ORCID iDs

Ariel Werle https://orcid.org/0000-0002-4382-8081
Bianca Poggianti https://orcid.org/0000-0001-8751-8360

Alessia Moretti https://orcid.org/0000-0002-1688-482X
Callum Bellhouse https://orcid.org/0000-0002-6179-8007
Benedetta Vulcani https://orcid.org/0000-0003-0980-1499
Marco Gullieuszik https://orcid.org/0000-0002-7296-9780
Mario Radovich https://orcid.org/0000-0002-3585-866X
Jacopo Fritz https://orcid.org/0000-0002-7042-1965
Alessandro Ignesti https://orcid.org/0000-0003-1581-0092
Johan Richard https://orcid.org/0000-0001-5492-1049
Geneviève Soucail https://orcid.org/0000-0001-9976-1237
Gustavo Bruzual https://orcid.org/0000-0002-6971-5755
Stephane Charlot https://orcid.org/0000-0003-3458-2275
Matilde Mingozzi https://orcid.org/0000-0003-2589-762X
Cecilia Bacchini https://orcid.org/0000-0002-8372-3428
Neven Tomicic https://orcid.org/0000-0002-8238-9210
Rory Smith https://orcid.org/0000-0001-5303-6830
Andrea Kulier https://orcid.org/0000-0002-0431-2445
Giorgia Peluso https://orcid.org/0000-0001-5766-7154
Andrea Franchetto https://orcid.org/0000-0001-9575-331X

References

Alatalo, K., Cales, S. L., Rich, J. A., et al. 2016, ApJS, 224, 38
Baldwin, J. A., Phillips, M. M., & Terlevich, R. 1981, PASP, 93, 5
Baron, D., Netzer, H., Prochaska, J. X., et al. 2018, MNRAS, 480, 3993
Bekki, K., Couch, W. J., Shioya, Y., & Vazdekis, A. 2005, MNRAS, 359, 949
Belli, S., Newman, A. B., & Ellis, R. S. 2019, ApJ, 874, 17
Blake, C., Pracy, M. B., Couch, W. J., et al. 2004, MNRAS, 355, 713
Boselli, A., Fossati, M., & Sun, M. 2021, arXiv:2109.13614
Bressan, A., Marigo, P., Girardi, L., et al. 2012, MNRAS, 427, 127
Bruzual, G., & Charlot, S. 2003, MNRAS, 344, 1000
Bundy, K., Bershady, M. A., Law, D. R., et al. 2015, ApJ, 798, 7
Cappellari, M. 2017, MNRAS, 466, 798
Cardelli, J. A., Clayton, G. C., & Mathis, J. S. 1989, ApJ, 345, 245
Chabrier, G. 2003, PASP, 115, 763
Charlot, S., & Fall, S. M. 2000, ApJ, 539, 718
Chauke, P., van der Wel, A., Pacifici, C., et al. 2019, ApJ, 877, 48
Chen, Y., Bressan, A., Girardi, L., et al. 2015, MNRAS, 452, 1068
Chen, Y.-M., Shi, Y., Wild, V., et al. 2019, MNRAS, 489, 5709
Cid Fernandes, R. 2007, IAUS, 241, 461
Cid Fernandes, R., Mateus, A., Sodré, L., Stasińska, G., & Gomes, J. M. 2005, MNRAS, 358, 363
Cid Fernandes, R., Stasińska, G., Schlickmann, M. S., et al. 2010, MNRAS, 403, 1036
Conroy, C. 2013, ARA&A, 51, 393
Couch, W. J., & Sharples, R. M. 1987, MNRAS, 229, 423
de los Reyes, M. A. C., & Kennicutt, Robert C., J. 2019, ApJ, 872, 16
de Sá-Freitas, C., Signorini Gonçalves, T., de Carvalho, R. R., et al. 2022, MNRAS, 509, 3889
D'Eugenio, C., Daddi, E., Gobat, R., et al. 2020, ApJL, 892, L2
D'Eugenio, F., van der Wel, A., Wu, P.-F., et al. 2020, MNRAS, 497, 389
Dressler, A., & Gunn, J. E. 1983, ApJ, 270, 7
Dressler, A., Oemler, A., Jr., Poggianti, B. M., et al. 2013, ApJ, 770, 62
Dressler, A., Smail, I., Poggianti, B. M., et al. 1999, ApJS, 122, 51
Ebeling, H., Edge, A. C., & Henry, J. P. 2001, ApJ, 553, 668
Ehlert, S., Allen, S. W., Brandt, W. N., et al. 2015, MNRAS, 446, 2709
Ferland, G. J., Chatzikos, M., Guzmán, F., et al. 2017, RMxAA, 53, 385
French, K. D. 2021, PASP, 133, 072001
Fritz, J., Poggianti, B. M., Bettoni, D., et al. 2007, A&A, 470, 137
Fritz, J., Poggianti, B. M., Cava, A., et al. 2011, A&A, 526, A45
Fritz, J., Poggianti, B. M., Cava, A., et al. 2014, A&A, 566, A32
Fritz, J., Moretti, A., Gullieuszik, M., et al. 2017, ApJ, 848, 132
George, K., Poggianti, B. M., Bellhouse, C., et al. 2019, MNRAS, 487, 3102
Gómez, P. L., Valkonen, L. E., Romer, A. K., et al. 2012, AJ, 144, 79
Goto, T. 2007, MNRAS, 381, 187
Gullieuszik, M., Poggianti, B. M., Moretti, A., et al. 2017, ApJ, 846, 27
Gunn, J. E., Gott, J., & Richard, I. 1972, ApJ, 176, 1
Kauffmann, G., Heckman, T. M., Tremonti, C., et al. 2003, MNRAS, 346, 1055
Kaviraj, S., Kirkby, L. A., Silk, J., & Sarzi, M. 2007, MNRAS, 382, 960
Kennicutt, Robert C., J., & De Los Reyes, M. A. C. 2021, ApJ, 908, 61
Kewley, L. J., Dopita, M. A., Sutherland, R. S., Heisler, C. A., & Trevena, J. 2001, ApJ, 556, 121
Kewley, L. J., Groves, B., Kauffmann, G., & Heckman, T. 2006, MNRAS, 372, 961
Larson, R. B., Tinsley, B. M., & Caldwell, C. N. 1980, ApJ, 237, 692
Leja, J., Carnall, A. C., Johnson, B. D., Conroy, C., & Speagle, J. S. 2019, ApJ, 876, 3
Lopes, P. A. A., Ribeiro, A. L. B., & Rembold, S. B. 2017, MNRAS, 472, 409
Lotz, J. M., Koekemoer, A., Coe, D., et al. 2017, ApJ, 837, 97
Moore, B., Katz, N., Lake, G., Dressler, A., & Oemler, A. 1996, Natur, 379, 613
Moretti, A., Radovich, M., Poggianti, B. M., et al. 2022, ApJ, 925, 4
Owers, M. S., Couch, W. J., Nulsen, P. E. J., & Randall, S. W. 2012, ApJL, 750, L23
Paccagnella, A., Vulcani, B., Poggianti, B. M., et al. 2019, MNRAS, 482, 881
Paccagnella, A., Vulcani, B., Poggianti, B. M., et al. 2017, ApJ, 838, 148
Pawlik, M. M., McAlpine, S., Trayford, J. W., et al. 2019, NatAs, 3, 440
Pawlik, M. M., Taj Aldeen, L., Wild, V., et al. 2018, MNRAS, 477, 1708
Peluso, G., Vulcani, B., Poggianti, B. M., et al. 2022, ApJ, 927, 130
Poggianti, B. M., Bridges, T. J., Komiyama, Y., et al. 2004, ApJ, 601, 197
Poggianti, B. M., Smail, I., Dressler, A., et al. 1999, ApJ, 518, 576
Poggianti, B. M., Aragón-Salamanca, A., Zaritsky, D., et al. 2009, ApJ, 693, 112
Poggianti, B. M., Jaffé, Y. L., Moretti, A., et al. 2017, Natur, 548, 304
Poggianti, B. M., Ignesti, A., Gitti, M., et al. 2019, ApJ, 887, 155
Postman, M., Coe, D., Benítez, N., et al. 2012, ApJS, 199, 25
Ricarte, A., Tremmel, M., Natarajan, P., & Quinn, T. 2020, ApJL, 895, L8
Richard, J., Claeyssens, A., Lagattuta, D., et al. 2021, A&A, 646, A83
Roman-Oliveira, F. V., Chies-Santos, A. L., Rodríguez del Pino, B., et al. 2019, MNRAS, 484, 892
Rowlands, K., Wild, V., Bourne, N., et al. 2018, MNRAS, 473, 1168
Saintonge, A., Kauffmann, G., Wang, J., et al. 2011, MNRAS, 415, 61
Sánchez, S. F., Avila-Reese, V., Hernandez-Toledo, H., et al. 2018, RMxAA, 54, 217
Sánchez-Blázquez, P., Peletier, R. F., Jiménez-Vicente, J., et al. 2006, MNRAS, 371, 703
Sanmartim, D., Storchi-Bergmann, T., & Brotherton, M. S. 2013, MNRAS, 428, 867
Sartoris, B., Biviano, A., Rosati, P., et al. 2020, A&A, 637, A34
Snyder, G. F., Cox, T. J., Hayward, C. C., Hernquist, L., & Jonsson, P. 2011, ApJ, 741, 77
Stasińska, G., Cid Fernandes, R., Mateus, A., Sodré, L., & Asari, N. V. 2006, MNRAS, 371, 972
Stuik, R., Bacon, R., Conzelmann, R., et al. 2006, NewAR, 49, 618
Tran, K.-V. H., Franx, M., Illingworth, G., Kelson, D. D., & van Dokkum, P. 2003, ApJ, 599, 865
Treu, T., Schmidt, K. B., Brammer, G. B., et al. 2015, ApJ, 812, 114
Tumlinson, J., Peeples, M. S., & Werk, J. K. 2017, ARA&A, 55, 389
Valdes, F., Gupta, R., Rose, J. A., Singh, H. P., & Bell, D. J. 2004, ApJS, 152, 251
Vulcani, B., Fritz, J., Poggianti, B. M., et al. 2020, ApJ, 892, 146
Wang, S., Liu, J., Qiu, Y., et al. 2016, ApJS, 224, 40
Werle, A., Cid Fernandes, R., Vale Asari, N., et al. 2019, MNRAS, 483, 2382
Werle, A., Cid Fernandes, R., Vale Asari, N., et al. 2020, MNRAS, 497, 3251
Wild, V., Almaini, O., Dunlop, J., et al. 2016, MNRAS, 463, 832
Wild, V., Kauffmann, G., Heckman, T., et al. 2007, MNRAS, 381, 543
Wild, V., Walcher, C. J., Johansson, P. H., et al. 2009, MNRAS, 395, 144
Wild, V., Almaini, O., Cirasuolo, M., et al. 2014, MNRAS, 440, 1880
Wild, V., Taj Aldeen, L., Carnall, A., et al. 2020, MNRAS, 494, 529
Wilkinson, A., Almaini, O., Wild, V., et al. 2021, MNRAS, 504, 4533
Yan, R., Newman, J. A., Faber, S. M., et al. 2006, ApJ, 648, 281
Yesuf, H. M., Faber, S. M., Trump, J. R., et al. 2014, ApJ, 792, 84
Zheng, Y., Wild, V., Lahén, N., et al. 2020, MNRAS, 498, 1259